In Vitro Analysis of Nanoparticulate Hydroxyapatite/Chitosan Composites as Potential Drug Delivery Platforms for the Sustained Release of Antibiotics in the Treatment of Osteomyelitis

VUK USKOKOVI and **TEJAL A. DESAI**

Therapeutic Micro and Nanotechnology Laboratory, Department of Bioengineering and Therapeutic Sciences, University of California, San Francisco, California 94158-2330

Abstract

Nanoparticulate composites of hydroxyapatite (HAp) and chitosan were synthesized by ultrasound-assisted sequential precipitation and characterized for their microstructure at the atomic scale, surface charge, drug release properties, and combined antibacterial and osteogenic response. Crystallinity of HAp nanoparticles was reduced because of the interference of the surface layers of chitosan with the dissolution/reprecipitation-mediated recrystallization mechanism that conditions the transition from the as-precipitated amorphous calcium phosphate phase to the most thermodynamically stable one—HAp. Embedment of 5–10 nm sized, narrowly dispersed HAp nanoparticles within the polymeric matrix mitigated the burst release of the small molecule model drug, fluorescein, bound to HAp by physisorption, and promoted sustained-release kinetics throughout the 3 weeks of release time. The addition of chitosan to the particulate drug carrier formulation, however, reduced the antibacterial efficacy against *S aureus*. Excellent cell spreading and proliferation of osteoblastic MC3T3-E1 cells evidenced on microscopic conglomerates of HAp nanoparticles *in vitro* also markedly diminished on HAp/chitosan composites. Mitochondrial dehydrogenase activity exhibited normal values only for HAp/chitosan particle concentrations of up to 2 mg/cm^2 and significantly dropped, by about 50%, at higher particle concentrations (4 and 8 mg/cm^2). The gene expression of osteocalcin, a mineralization inductor, and the transcription factor *Runx2* was downregulated in cells incubated in the presence of 3 mg/cm^2 HAp/chitosan composite particles, whereas the expression of osteopontin, a potent mineralization inhibitor, was upregulated, further demonstrating the partially unfavorable osteoblastic cell response to the given particles. The peak in the expression of osteogenic markers paralleling the osteoblastic differentiation was also delayed most for the cell population incubated with HAp/chitosan particles. Overall, the positive effect of chitosan coating on the drug elution profile of HAp nanoparticles as carriers for the controlled delivery of antibiotics in the treatment of osteomyelitis was compensated for by the lower bacteriostatic efficiency and the comparatively unviable cell response to the composite material, especially at higher dosages.

Correspondence to: Vuk Uskokovi (Telephone: +415-4120233; vuk21@yahoo.com).

INTRODUCTION

Osteomyelitis, infectious inflammation of bone,[1] targets a considerable number of patients, particularly among the three most critical populations: children, elders, and inhabitants of Third World countries. The mainstay therapy for this comparatively rare disease with the incidence of approximately 1%–2% in the USA[2] has consisted of: (1) intravenous administration of antibiotics for 2–6 weeks depending on the severity of the infection, frequently followed by a 6-month course of oral antibiotics in the case of chronic osteomyelitis, and (2) surgical debridement of the portion of bone that has undergone necrosis because of the restriction of blood flow by the formed abscesses.[3,4] The immediate downsides of this traditional therapy include: (1) the side effects and cost-ineffectiveness of systemic administration of antibiotics; (2) low concentration of the therapeutic agent around the site of infection consequential to obstructed vasculature, prone to induce the resistance of the pathogen to the antibiotic therapy; and (c) irretrievable bone loss that often demands insertion of implants or prostheses as lasting bone substitutes.

It is believed that although local and sustained release of the drug could overcome the need for prolonged antibiotic therapies, induction of osteogenesis by the carrier itself could accelerate the bone healing process and minimize the extent of the surgical removal of affected bone, along with skeletal deformations and unaesthetic physical disfigurement entailed by it. Moreover, as the surgical implantation of orthopedic substitutes presents a major source of infection in the clinical setting, with the postoperational infection rates ranging from 1% to 3% for primary joint replacement[5] to 15% for primary knee surgeries[6] to up to 50% for open fracture revisions of tibia,[7] there is a great demand to develop prophylactic materials as either intrinsic components of regular implants or space-filling adjuvants that would facilitate surgical implantation.

Be it prophylactic or remedial, one such drug delivery platform that is simultaneously antibiotic and osteogenic, if developed, would present a big step forward in finding ways to improve the conventional approach to prevention and treatment of osteomyelitis. In our previous studies, we have shown that various stoichiometric forms of calcium phosphate, the natural constituent of bone, can be used as viable osteoinductive carriers for the delivery of antibiotics.[8] The sustained release of small molecule drugs from calcium phosphate particles was, however, shown to be contingent on the formation of solid blocks through desiccation.[9] For the fabrication of injectable nanoparticulate calcium–phosphate-based gels as drug carriers, the dispersability of the particles is required, but it comes at the cost of accelerated release of the drug. In this work, we attempt to overcome this issue and promote more sustained drug release profiles by coating the drug-containing surface of hydroxyapatite (HAp) nanoparticles with a marine fiber, chitosan. Because of their ability to (1) act as plasticizers, (2) protect the drug depots residing on the particle surface from the premature,

burst release, and (3) provide a stable surface that could be chemically functionalized with various targeting, therapeutic or diagnostic ligands, polymers have been the prime choice of additives to calcium–phosphate-based composites for bone-filling applications.[10]

The application of chitosan, a linear polysaccharide and a copolymer of D-glucosamine and N-acetyl-D-glucosamine, as a potential drug and/or gene delivery carrier has been attracting attention over the last two decades because of the facts that: (1) chitosan is a naturally derived polymer, the second most abundant organic material next to cellulose, and easily extractable from fungal cell walls and crustacean shells, the byproducts of the food industry[11]; (2) it has a range of bioactivities ascribed to it, including antimicrobial, antitumor, anti-inflammatory, and immunity enhancing ones[12–15]; (3) it is a cationic polymer able to bind the typically negatively charged biomolecular moieties and transfect cells,[16–18] alongside finding use in water purification industry as an adsorbent of pollutants[19]; (4) it is mucoadhesive and capable of increasing the permeability of epithelial monolayers to various drugs[20,21]; and (5) it is approved by the US FDA and is available as a regular fibrous supplement in diet.[22] Composites of HAp with chitosan as potential drug delivery carriers have been synthesized before in different forms: with HAp (1) coated by the polymer,[23,24] and (2) dispersed within chitosan-based polymeric matrices.[25–28] Systematic analyses of the controlled release of antibiotics[29–33] or other small molecules[34–36] from these composites have been far rarer, especially when coupled to the analysis of their antibacterial and osteoconductive potencies. One such combined analysis of drug elution profiles and antibacterial and osteogenic performance of HAp/chitosan composites has presented the central topic of this study.

MATERIALS AND METHODS

Synthesis and Characterization of HAp Nanopowders and HAp/Chitosan Composite Nanoparticles Loaded with the Drug

Narrowly dispersed spherical HAp nanoparticles were prepared by adding 200 mL of 0.06 M aqueous solution of $NH_4H_2PO_4$ containing 12.5 mL 28% NH_4OH dropwise (13 mL/min) to the same volume of 0.1 M aqueous solution of $Ca(NO_3)_2$ containing 25 mL 28% NH_4OH at 37°C, vigorously agitated in an ultrasound field using a Q700 (QSonica, New-town, CN) ultrasonicator, a regular tip, half an inch in diameter (1.3 cm), the amplitude equal to 20 and pulse on/off time of 2/1 s. After the addition of $NH_4H_2PO_4$ was complete, the resulting suspension was cooled down to room temperature and either clindamycin phosphate (Tokyo Chemical Industry, Tokyo, Japan) in the amount of 100 mg or 0.2 mg fluorescein–Na (Sigma, Dorset, UK) was added to it, followed by aging for 1 h. To coat thus-obtained HAp nanoparticles with chitosan [poly(D-glucosamine) deacetylated chitin, M_w = 190–310 kDa; Sigma], 10 mL of 1 mg/mL chitosan solution in 30 mM HCl was then gradually, over 10 min, added to the sol agitated using the abovementioned ultrasonication conditions. The precipitate alongside its parent solution was left to age in the atmospheric conditions for 1 h. After the given time, the precipitate was washed once with deionized (DI) H_2O, centrifuged (5 min at 3500 rpm), and dried in a vacuum oven (Isotemp 280A; $p = -20$ mmHg) at 60°C.

Prior to the ultrastructural analysis by means of the high-resolution transmission electron microscopy (HR-TEM), the samples were dispersed in 50:50 (vol) mixture of phosphate-

buffered saline (PBS) and ethanol, vortexed and a droplet of the resulting dispersion was smeared on top of a carbon-coated copper grid (Ted Pella, Redding, CA). After 1 min, the excess liquid was blotted off with filter paper, after which negative staining was performed by depositing a droplet of 1% aqueous solution of phosphotungstic acid in 30 mM NaOH (pH 6.7) on top of the grids. Following 1 min incubation in air, the excess liquid was blotted off and the grids were left to dry in air. The samples were subsequently stored and then analyzed on a (FEI, Hillsboro, OR) monochromated F20 UT Tecnai HR-TEM under the electron acceleration voltage of 200 kV.

The phase composition of HAp particles was confirmed on a (Bruker, Billerica, MA) AXS D4 Endeavour X-ray diffractometer. Interplanar distances (d) with strongest reflections on X-ray diffractograms were correlated with Miller indices {hkl}, the diffraction angle (θ) and lattice parameters for the hexagonal lattice of HAp (P63/m space group; $a = 0.937$ nm and $c = 0.688$ nm) using the following equations:

$$\lambda = 2d_{\text{hkl}}\sin\theta_{\text{hkl}} \quad (1)$$

$$1/d_{\text{hkl}}^2 = 4/3((h^2 + hk + 1^2)/a^2) + 1^2/c^2 \quad (2)$$

The average crystallite diameter (r) was estimated by applying Debye–Scherrer's equation on the half-width of (211) diffraction peak of HAp in radians ($\beta_{1/2}$), the diffraction angle (θ), and 1.5418 Å as the wavelength of $Cu_{K\alpha}$ as the radiation source (λ):

$$r = 0.94\lambda/\beta_{1/2}\cos\theta \quad (3)$$

The ξ-potential analysis was carried out on a Zetasizer Nano Series (Malvern, Worceslershire, UK) dynamic light scattering device. The analyzed powders were initially suspended in 20 mM Tris–HCl solution (pH 7.4). Zeta potential values were measured at room temperature and at different pH values in the range 4.5–11.5, obtained by adding small volumes (1–3 μL) of 1 N HCl or NaOH. The volume of each suspension was 700 μL and the results of each measurement were averaged over 100 runs at acquisition times of approximately 10 s. The universal dip cell (Malvern) with a removable palladium electrode and the spacing of 2 mm in disposable glass cuvettes was used for measurements. The voltage was automatically set to 1.2 V and the Smoluchowski model was applied for the conversion of the electrophoretic mobility values to ξ-potentials:

$$\xi = \eta\nu/\varepsilon E = \eta\mu/\varepsilon (V) \quad (4)$$

where η is the viscosity coefficient of the medium, ν is the electrophoretic velocity, μ is the electrophoretic mobility, ε is the dielectric constant of the medium, and E is the gradient of the electric field applied.

Drug Release

Drug release experiments were conducted by immersing 1 mg of fluorescein-loaded HAp and HAp/chitosan powders, separately, in 300 μL of 20 mM Tris–HCl (pH 7.4) in capped microfuge tubes, and incubating it at room temperature under mild agitation (60 rpm on a shaker plate) for up to 3 weeks. Every 24–48 h, 100 μL aliquots were sampled out and analyzed for fluorescence (Packard Fluorocount, $\lambda_{excitation}$ = 495 nm, $\lambda_{emission}$ = 525 nm) convertible to the concentration of the released fluorophore, before being replaced with fresh medium to prevent its saturation. At the end of 3 weeks of release time, the remaining powders were dissolved in 20 mM HCl. The resulting fluorescence was measured and used to calculate the overall amount of the drug initially contained by the powders. The drug released at each time point was then normalized to the overall amount of the released drug. Each sample was analyzed in triplicates and the fluorescence of each experimental replica was determined as the average of three independent measurements.

Bacterial Culture

A single colony of *Staphylococcus aureus* (subspecies *aureus* Rosenbach; ATCC 25923) cultured on a blood agar plate over 48 h was stabbed with a pipette tip, which was then placed in 5 mL of 37 mg/mL brain heart infusion (BHI) broth and kept on an incubator shaker (Innova 44) overnight at 37°C and 225 rpm. The turbid broth was collected the following day and 8 mL of it was added to serially diluted samples containing different concentrations of different clindamycin-loaded powders in 1 mL of 37 mg/mL BHI broth, for the purpose of determining the minimal inhibitory concentration (MIC) of the antibiotic-containing powders under the given analytical conditions. The given bacterial concentration (1:125,000 of 5 mL 37 mg/mL BHI broth inoculated overnight with a single bacterial colony) was found to be equal to the standard concentration of 10^5 bacteria per milliliter after comparing the optical density at λ = 600 nm of a range of serially diluted bacterial broths with 0.5 M Mc-Farland solution (equivalent to approximately 10^8 bacteria per milliliter) prepared by mixing 1% $BaCl_2$ solution and 1% H_2SO_4 in the volume ratio of 1:200, respectively. The dilution yielding the same absorbance as that of 0.5 M McFarland solution was diluted 10^3 times to yield the standard bacterial concentration of 10^5 bacteria per milliliter. The series of samples was incubated overnight on the incubator shaker and visually analyzed the following day for their turbidity and the optical density at λ = 600 nm. Turbid broths indicated those in which the concentration of the antibiotic released from the particles was insufficient to prevent the bacterial growth, as opposed to the transparent broths. A parallel antibacterial test using a modified Kirby–Bauer method was repeated on sheep blood agar plates (UCSF Cell Culture Facility). A freshly inoculated bacterial broth was diluted to the concentration of 10^8 cfu/mL and 200 μL of it was added to the plate and spread until the surface was fully covered. One milligram of the clindamycin-loaded particles was then added onto the plate in form of separate islets. The plates were incubated overnight at 37°C and observed for inhibition of bacterial growth around the nanoparticulate samples the following day. All the experiments were carried out in quadruplicates and compared with the negative controls, incubated without any added bacteria and the positive controls, incubated with bacteria and no antibiotic-loaded particles.

Cell Culture

Mouse calvarial preosteoblastic cell line, MC3T3-E1 subclone 4, was purchased from American Tissue Culture Collection (ATCC; Rockville, Maryland) and cultured in Alpha Minimum Essential Medium (α-MEM; Gibco, Carlsbad, CA) supplemented with 10% fetal bovine serum (FBS; Invitrogen, Carls-bad, CA) and no ascorbic acid (AA). The medium was replaced every 48 h, and the cultures were incubated at 37°C in a humidified atmosphere containing 5% CO_2. Every 7 days, the cells were detached from the surface of the 75 cm^2 cell culture flask (Greiner Bio-One, Monroe, NC) using 0.25 wt % trypsin, washed, centrifuged (1000 rpm × 3 min), resuspended in 10 mL α-MEM and subcultured in 1:7 volume ratio. Cell passages 17–21 were used for the experiments reported hereby. The cultures were regularly examined under an optical microscope to monitor growth and possible contamination.

For the purpose of staining with fluorescent markers, MC3T3-E1 cells were seeded on glass cover slips placed in 24-well plates and 500 μL of α-MEM supplemented with 10% FBS, (Invitrogen) and no AA at the density of 6×10^4 cells per well. After 5 days of incubation, nearly confluent cells were treated with α-MEM containing 50 μg/mL AA as the mineralization inductor. At the same time, 2–4 mg/cm^2 of particles were added to the cells. After 5 days of incubation in the presence of the drug-containing particles, cells were stained for f-actin and nucleus. The staining procedure began with washing the cells with PBS (pH 7.4) and fixing them for 15 min in 3.7% paraformaldehyde. The cells were then washed with PBS 3 × 5 min and then with the blocking solution (PBT = 1% bovine serum albumin, 0.1% Triton X-100 in PBS) 2 × 5 min. The cells were then blocked and permeabilized in PBT for 1 h, and then incubated in 20 μg/mL 4′,6-diamidino-2-phenylindole dihydrochloride nuclear counterstain (Invitrogen), 2 μM calcein AM as HAp-particle-staining compound, and 10 μg/mL phalloidin-tetramethylrhodamine (AlexaFluor 555; Invitrogen), all in PBT for 1 h and then washed with PBS 3 × 5 min. The cover slips containing the fixed and stained cells were mounted onto glass slides using hard set vectashield and nail polish and were subsequently imaged on a confocal laser scanning microscope–C1si (UCSF Nikon Imaging Center, San Francisco, CA) at 20–100× magnification in oil. The final images were obtained by z-stack volume-rendering 15–20 raw images spaced by 1 μm. All the experiments were performed in triplicates.

For the purpose of MTT [3-(4, 5-dimethylthiazol-2-yl)-2, 5-diphenyl tetrazolium bromide] *in vitro* toxicological assay, MC3T3-E1 cells were seeded in 48-well plates at the density of 3×10^4 cells per well and cultured in the abovementioned AA-free medium until confluency was reached. The AA-free medium was then substituted with the AA-supplemented medium and, at the same time, different amounts of particles were added to the cells, in the range of 2–8 mg/cm^2. At the end of the incubation period, which lasted for 24 and 96 h, 20 μL of 5 mg/mL MTT (M-5655; Sigma) in PBS were added to each well. After 4 h of incubation at 37°C, 220 μL of MTT solubilization solution (M-5655; Sigma) were added to each well. Following an additional 2 h incubation of softly shaken wells (60 rpm) at room temperature, 100 μL aliquots from each well were analyzed for absorbance at 570 nm on a UV/Vis spectrophotometric microplate reader (Spectra Max 190; Molecular Devices). All the

particle types were analyzed in biological sextuplicates and the resulting absorbance values were normalized to the negative control.

To run a real-time polymerase chain reaction (qPCR) analysis, MC3T3-E1 cells were first seeded in 96 well plates at the density of 3×10^4 cells per well and cultured in the abovementioned AA-free medium until confluency was reached. The AA-free medium was then substituted with the AA-supplemented medium and, at the same time, 1 mg of particles was added to each well. At the end of the incubation period, which lasted for either 5 or 10 days, cell lysis, reverse transcription (Bio-Rad, Harcules, CA) and qPCR (StepONEPlus; Applied Biosystems) were performed using the Fast SYBR Green Cells-to-CT kit (Ambion) in accordance with the manufacturer's instructions. Each experiment was performed in triplicates and each experimental replica was analyzed for mRNA expression in triplicates too ($n = 3 \times 3$). The expressions of one housekeeping gene, β-actin (*ACTB*), and three osteogenic markers, osteocalcin (*BGLAP*), osteopontin (*BSP-1*), and *Runx2* were analyzed. Table 1 shows the primer pair sequences used.[37–39] The real-time PCR results were analyzed using the C_t method [40] and all the data were normalized to *ACTB* expression levels.

RESULTS AND DISCUSSION

Sizes, morphologies, and phase distribution profiles for HAp nanoparticles alone and in combination with chitosan can be seen from the transmission electron micrographs displayed in Figure 1. Although HAp nanoparticles precipitated and dried without the presence of chitosan formed large-scale aggregates (Figs. 1a–1c), a much greater level of their dispersability was achieved upon coprecipitation with chitosan (Figs. 1e–1f). Round HAp particles with relatively sharp edges, quasihexagonal shapes, and narrowly dispersed sizes, ranging from 2 to 10 nm were detected in both samples. The ultrastructural characterization by means of HR-TEM resulted in the discernment of individual crystal planes with structural parameters typical for hexagonal HAp with P6₃/m space group. The lattice spacing characteristic of HAp crystal symmetry is visible in Figure 1e, including that of the hexagonal, (001) plane ($d_{001} = 0.527$ nm), and a range of similar interplanar distances parallel with the *c*-axis [(001)]—(100), (110), (010), (210)—indicating random orientation of the crystallites embedded in the chitosan matrix. As expected, the most prominent plane on the surface of the composite corresponded to (002) plane, perpendicular to the c-axis of hexagonal crystals, with the characteristic spacing of 0.264 nm (Fig. 1e). As a result of the application of the ultrasound and thus-achieved good dispersability of precipitated HAp nanoparticles, the crystalline domains appeared to be well dispersed within the amorphous polymeric matrix (Fig. 1e). Observed were neither the areas of extensive aggregation of the ceramic phase nor ceramic-free polymeric regions. The number of HAp particles encapsulated by the polymer ranged widely from one (~10–20 nm in diameter; inlet of Fig. 1d) to hundreds (~300 nm in diameter; Fig. 1d). The monophasic composition of the precipitated HAp was confirmed using X-ray diffraction (Fig. 2). The narrow half-width of the most intensive, (211), reflection indicated comparatively high crystallinity of the ceramic phase, considering the small, sub-10-nm particle sizes. In fact, Debye–Scherrer's equation applied on this peak estimated the average HAp crystallite size at 8.4 nm, indicating an exceptionally small proportion of amorphous surface layers compared with the crystalline

bulk of the particles. The thermal energy introduced in the system with the intense ultrasound is expected to have been crucial in promoting both the excellent crystallinity and dispersability of the resulting nanoparticles.

Both coating of the as-precipitated HAp particles with chitosan and adsorption of clindamycin onto them was shown to reduce their crystallinity (Fig. 2). The average crystallite size estimated using Eq.(3) dropped approximately 30%, down to 5.8 and 5.9 nm upon coating with chitosan and the adsorption of clindamycin, respectively. Furthermore, as could be seen from Figure 2a, whereas three distinct diffraction peaks are observed in the 30°–35° region of 2θ for pure HAp, only a broad peak corresponding to the major, (211), reflection is seen in the X-ray diffractogram of HAp coated with chitosan (Fig. 2b). Similarly, in the 45°–55° region of 2θ, pure HAp exhibits four distinct peaks—(222), (130), (213), and (004)—whereas only weak (213) and (004) reflections, almost merged with the baseline, are seen in the diffractogram of HAp/chitosan (Fig. 2b). This effect is consequential to the hindered recrystallization of as-precipitated calcium phosphate particles with increasing their aging time in the solution. The first phase to precipitate from a solution supersaturated with respect to calcium phosphate is an amorphous calcium phosphate phase.[41–43] Following the Ostwald–Lussac kinetic principle, which dictates sequential progression from the least thermodynamically stable phase to the most stable one for which the supersaturation ratio exceeds 1, this initially formed amorphous phase transforms into the most stable calcium phosphate phase, HAp, in a process whose time scale varies from seconds to hours, depending on the solution parameters, including, most importantly, pH, temperature, polarity of the precipitation medium, and the concentration and identity of foreign ions. The chitosan molecules bound to the particle surface interfere with the dissolution/reprecipitation mechanism that conditions this transition[44] and reduce the crystallinity of the particles. The same, although less prominent effect was observed upon the addition of clindamycin to the as-precipitated HAp particle suspension (Fig. 2c), which is similarly explained by the rapid adsorption of the antibiotic molecules onto the particle surface. Two diffraction peaks originating from chitosan were detected in the X-ray diffractograms of the composites, concordant with the mainly matrix-like nature of the latter, where sufficiently sized chitosan molecule aggregates existed to allow for the crystalline order to be established.

Successful coating of HAp particles with chitosan was confirmed using ξ-potential measurements. As shown in Figure 3, coating of HAp particles with chitosan resulted in the shift of ξ-potential toward more positive values, typically by 10–15 mV higher than for HAp at any given pH. The negative charge on the surface of HAp particles at pH greater than 6.7 is an indication of their crystalline nature,[45] as the transition from neutral or positive values to negative ones reflects the amorphous-to-crystalline transition that presumably all calcium phosphate precipitates pass *en route* to the final and the most thermodynamically stable, apatite phase. As a result of cationic glycopolymeric moieties (i.e., finite degree of protonation of 2-amino groups of D-glucosamine units at physiological pH), the building blocks of chitosan molecules, chitosan is typified by positive zeta potentials.[46–48] Not only does this surface charge propensity make chitosan capable of opening the tight junctions between epithelial cells,[49] but it also boosts the cell penetration potency of chitosan

particles,[50] in analogy with the role played by polysaccharides residing on the surface of gram-negative bacteria.[51] The deprotonation of the amine groups (pK_a 6–6.5[52]; $NH_3^+ \rightarrow$ NH_2) on the surface of chitosan particles is, however, responsible for shift to negative ξ-potential at pH values that exceed the isoelectric point (IEP) of approximately 7.9, approximately one unit higher than that of pure HAp (6.7). Finally, as seen from Figure 3, following the 3-week degradation period of HAp/chitosan composite particles in the solution, the ξ-potential at the physiological pH decreases compared with the value characteristic of the initial, as-prepared HAp/chitosan particles (3.9 → 0.9 mV), approaching the negative ξ-potential of pure HAp (−7 mV) and correlating with the degradation of the polymeric layers and the exposition of the core HAp particles to the solvent. Correspondingly, the IEP of HAp/chitosan composite decreases from 7.9 to 7.5 following the polymer degradation and drug release, approaching the IEP of pure HAp: 6.7 (Table 2).

Comparative profiles for the drug release of fluorescein from HAp nanoparticles and HAp/ chitosan composites are presented in Figure 4a. The addition of chitosan mitigated the burst release of the drug adsorbed on the surface of HAp. Thus, only 15% of the drug was released from HAp/chitosan in the first 24 h and 50% in the first week of the release time, as opposed to 60% of the drug being released from pure HAp in the first 24 h and 75% in the first 48 h. The release from chitosan-stabilized HAp followed a very low kinetic order of release throughout the entire 3-week release period, equaling zero for the first 4 days of release and for the release period between days 4 and 21, though with approximately twice higher release rate in the 0–72 h period than for the 7–21 day time range. Solid fitting of the kinetics of fluorescein release from HAp/chitosan for the first 72 h and for the period between 7 and 21 days to a linear regression model is also displayed in Figure 4. Different release kinetics observed for HAp alone and HAp in combination with chitosan imply different release mechanisms, defined by the slowest kinetic step: surface desorption in the former case and diffusion of the drug through the polymeric network and/or degradation of the polymer in the latter case. Depending on crystallinity, the degrees of cross-linking and deacetylation, molecular weight (M_w), drug-to-polymer ratio, temperature and particularly pH of the local environment, the degradation kinetics of chitosan particles, and the release rate of the encapsulated drug could be find anywhere in the range of hours[53] to days[54] to weeks[55] to months[56] or even longer.[57] Similarly to other biopolymers, chitosan degrades in two stages, the first of which is induced by water uptake, swelling of the polymer and leaching of low M_w polymeric chains, typically lasting for a week, whereas the second one involves hydrolytic degradation and on most occasions occurs no sooner than 2 weeks after the immersion.[58] Water uptake is known to result in extensive pore formation and a consequent increase in the drug release rate.[59] This may explain for the fact that although coating with chitosan managed to suppress the burst release, it did not extend the release timescale beyond the 3-week window provided by HAp as the drug carrier *per se*. The transition from the swelling-induced degradation to the hydrolysis-controlled one presumably corresponds to the change in the slope of the temporal drug release curve (Fig. 4) around the days 5–7.

The results of testing the particles for their antibacterial activity against *S aureus* in BHI broths are shown in Figure 5. Unlike HAp particles loaded with clindamycin using the

physisorption effect, which showed high effectiveness in suppressing the bacterial growth, with the MIC of less than 1 mg/mL, stabilization of the given antibiotic-loaded particles with the surface layer of chitosan markedly diminished their antibacterial activity, as evidenced by the corresponding increase of their MIC to less than 32 mg/mL. The same tests carried out on agar plates (Fig. 6) confirmed a gradual decrease in the antibacterial effectiveness from pure clindamycin to clindamycin-loaded HAp to clindamycin-loaded HAp/chitosan. Surprisingly, the addition of the same amount of clindamycin and clindamycin-loaded HAp onto infected agar plates resulted in only approximately twice smaller inhibition zone around clindamycin-loaded HAp compared with that around pure clindamycin, indicating excellent antibacterial efficacy of antibiotic-loaded HAp. On the contrary, the inhibition zone around 5 mg of HAp/chitosan loaded with clindamycin was smaller than that around 1 mg of clindamycin-loaded HAp. The more sustained release of the antibiotic from HAp/chitosan led not to expansion, but progressive shrinkage of the inhibition zone, by approximately 20% between 24 and 72 h. In contrast, the inhibition zone around clindamycin-loaded HAp increased by 40% in the same period of time. The significantly higher antibacterial efficacy of clindamycin-loaded HAp particles compared with clindamycin-loaded HAp/chitosan can be explained by the faster release of the antibiotic molecules off the particle surface in the absence of the chitosan layer that stabilizes against the burst release. The tradeoff between a more sustained drug release profile and a lower antibacterial efficacy can thus be immediately noticed. The released mass of fluorescein after the 3-week period of release was the same (60 μg of drug per milligram of carrier) for both HAp and HAp/chitosan, suggesting that antibiotic molecules were not expelled from the HAp particle surface during the coating process and that the lower antimicrobial efficacy of antibiotic-loaded HAp/chitosan is mainly because of the lower initial release of the drug. In addition, (1) the drug release solution, (2) the freshly inoculated broths, and (3) the broths in which the bacterial growth was inhibited by either of the powders all had identical pHs (7.4), which discards the possibility of increased entrapment of the drug because of a greater degree of protonation of chitosan amine groups at lower pHs that favor bacterial growth. In our former study, we showed a satisfactory antibacterial effect of clindamycin-carrying HAp nanoparticles coated with poly-lactide-co-glycolide (PLGA), with the MIC of only 1–2 mg/mL.[60] The overnight growth of *S aureus* in BHI broths elevated their pH to 8.2, suggesting that alkaline residues of chitosan molecules might have a less positive effect on suppressing the growth of this particular strain than the acidic residues of PLGA. Unlike PLGA, whose surface the acidic monomers render negatively charged under physiological conditions, amino-glycopolymeric chitosan is positively charged. Adsorption of clindamycin onto HAp particles increased their ξ-potential in water and at pH 7.4 from −7 to +7.6 mV. Consequently, from the electrostatic attraction point of view, although the antibiotic molecules would more readily redisperse in the acidic PLGA layer, they would tend to remain tightly bound to the core particle (HAp) surface, which would delay their release during the polymer degradation stage. The potential advantage of the usage of chitosan in terms of its antibacterial performance was, however, meant to come from its positive surface charge.[61–63] Yet, as demonstrated by the agar plate experiments, chitosan-coated HAp *per se* did not exhibit any substantial antibacterial effect against *S aureus* (Fig. 6d). Another possibility is that the synergy between the antibiotic and its carrier, in this case HAp/chitosan, accounted for the lower antimicrobial efficacy, which,

if true, may have been because of the retention of the drug in the surface layers of particles formed by erosion of the composite, perhaps protected by the aforementioned strong polymer–ceramic interaction, where it could be picked by the signal from the fluorescent detector, yet remain unavailable to neutralize the ribosomal RNA of the bacterium.

Confocal images obtained on immunofluorescently stained osteoblastic cells incubated with HAp and HAp/chitosan particles are shown in Figure 7. The osteoblastic cells were shown to engage in an intimate contact with HAp particles. Single-plane images demonstrate extensive cell spreading along the sides of microscopic particle conglomerates of pure HAp, directly indicating osteoconductivity of the solid phase. Moreover, cytoskeletal microfilaments adopted healthy, striated morphologies, indicating a satisfactory osteoblastic response to the given material. Incubation of the cells with HAp/chitosan, however, induced a less positive osteoblastic response. Cell proliferation appeared to have been somewhat reduced and no intimate contact such as that achieved at the interface between osteoblastic cells and pure HAp was visible for HAp/chitosan composites, suggesting their lesser osteoconductivity compared with that of pure HAp. The elastic modulus of osteoblasts, estimated at around 20 kPa, is larger than that of fibroblasts (3 kPa) and the mechanoreciprocity principle dictates that osteoblast proliferation will be higher on stiffer extracellular matrices and material surfaces.[64] This may explain why a more intimate contact was observed for osteoblastic cells on HAp particles, whose Young's tensile modulus was measured by nanoindentation at approximately 120 GPa,[65] rather than on less stiff chitosan (~3 GPa).[66] A markedly better contact observed at the HAp/osteoblast interface than at the one between HAp/chitosan and osteoblasts could also be explained by the fact that the chemical composition of HAp is practically identical to the mineral phase of bone, if we were not to account for ionic impurities present in biological apatite. The higher roughness of the surface of HAp compared with that of chitosan can also be a factor that contributed to the more intimate contact of osteoblasts with the former phase, as earlier studies have demonstrated a direct proportionality between the cellular proliferation and the nanoscale coarseness of the substrates.[67,68]

These insights were confirmed in the measurements of the cell mitochondrial dehydrogenase activity, directly indicative of cell viability (Fig. 8a). Namely, incubation with moderate particle concentrations yielded equally proliferating cells as those comprising the control sample, but any HAp/chitosan particle concentration higher than 2–4 mg/cm^2 resulted in twofold drops in the mitochondrial activity. This concentration range corresponds to 15–30 mg/mL when normalized to the volume of the cell culture medium, the upper limit of which was the amount required to suppress the standard concentration of *S aureus* colony forming units suspended in broth (10^5 per milliliter; Fig. 5) from growing. This suggests that the amount of clindamycin-loaded HAp/chitosan required to suppress the bacterial growth *in vivo* would probably have a somewhat unviable effect on osteoblasts that populate the infected milieu. In contrast, no significant changes in cell viability were detected upon incubation of osteoblastic cells with the identical amounts of HAp particles. Increased cell growth inhibition was previously noticed to occur in parallel with the onset of chitosan degradation.[69] Products of degradation of chitosan include glucosamine and various oligosaccharides able to activate the production of reactive oxygen species and thus inhibit

the proliferation of tumor cells (the category to which MC3T3-E1 cell line utilized in this study also belongs), being one of the reasons why chitosan has been widely considered to be anti-cancerous. By facilitating the nanoparticle uptake by the cell, the positive surface charge of chitosan may have presented an additional factor that determined the low cell viability outcome at higher particle concentrations.[70] An earlier study has concordantly demonstrated that chitosan nanoparticles in the same size range as the one used in our work (10–300 nm) were extensively internalized by the human epithelial Caco-2 cells via clathrin-mediated endocytosis,[71] imposing visible damage to the organelles and enhancing the paracellular transport of the drug along the way.[72] Other studies, particularly on nanosized particles, could reiterate these findings of the ability of polycationic chitosan to compromise the cell membrane integrity and promote cytotoxocity, and that on an array of cell types, from human hepatocytes[73] to human intestinal cells[74–76] to human gastric cells[77] to mouse melanoma cells.[78] As for *in vivo* tests, although the majority of studies have shown no harmful effects of the oral consumption of chitosan[79] except following long-term intake (>12 weeks),[80] reports claiming that chitosan administered orally and intraperitoneally to mice induces hyperplasia to foreign body giant cells in the spleen[81] and causes other cellular and physiological abnormalities[82,83] could be found in the literature too.

Expression of osteogenic markers typifies the onset of osteogenetic activity of bone cells and parallels the subsequent mineralization events. Formerly, qPCR studies have demonstrated a more elevated expression of *Col I, Runx2, ALP,* and *BGLAP* in both mouse C3H10T1/2 and human alveolar bone-marrow-derived mesenchymal stem cells cultured on HAp/chitosan than in those cultured on chitosan only.[84,85] Our previous gene expression studies have evidenced the ability of nanocrystalline HAp to upregulate these very same osteogenic markers with respect to the controls grown on standard cell culture plastics.[8] The addition of the nanoparticulate HAp prepared in this study to cultured MC3T3-E1 cells, however, did not produce statistically significant changes in the expression of two of the osteogenic markers analyzed: *BGLAP* and *Runx2* (Fig. 8b). *BGLAP* is a gene encoding for osteocalcin, a protein that is a potent promoter for nucleation of biominerals, whereas *Runx2* is a key transcription factor involved in the differentiation of osteoblasts. Studies have shown that *Runx2* knockout mice completely lose the ability to differentiate mesenchymal cells to osteoblasts.[86] Interestingly, the smaller size of HAp nanoparticles applied in this study compared with those used earlier[8]—10–20 versus 20–100 nm—produced a less favorable effect on the osteogenic activity of MC3T3-E1 cells, despite the fact that it more closely resembled the dimensions of the apatite platelets in bone: $30 \times 20 \times 2$ nm^3.[87] This effect could be explained by a larger uptake of the particles with lower sizes. The particle size determines the type and efficiency of the transport of nanoparticles across the cell membrane, which, in turn, codefines the effects that they will exert on the cell.[88] Although the intracellular presence of HAp crystals similar in size and shape to those that present the outcomes of internal mineralization may slow down the osteogenic activity of the cell, the binding of the cell to a more stable HAp surface may produce the opposite effect. The mRNA expression of the more ambiguous osteogenic marker, *BSP-1*, which encodes for osteopontin, the protein that acts as a mineralization inhibitor, increased threefold for cells incubated with HAp and 100-fold for cells incubated with HAp/chitosan. In addition to its marking mineralization events, *BSP-1* is also a negative regulator of proliferation and

differentiation in MC3T3-E1 cells[89] and its dramatic upregulation for cells incubated with HAp/chitosan is in agreement with their lower viability (Fig. 8a) as well as with a 12-fold lower expression of the housekeeping gene, *ACTB*, compared with the control. Moreover, as shown in Figure 8c, the 10-to-5-day postdifferentiation ratio in the mRNA expression levels of *BGLAP* and *Runx2* was highest for the cells incubated with HAp/chitosan. Expression of the two osteogenic markers in MC3T3-E1 cells is known to peak around day 5 after the addition of differentiation agents. Any interruption of the differentiation of MC3T3-E1 fibroblasts to osteoblast-like cells becomes evident in the delayed peaking of the expression of osteogenic markers. This all speaks in favor of a more favorable effect of HAp than HAp/chitosan composites on the bone-forming activity of the osteoblastic cells.

CONCLUSIONS

In this study, an attempt was made to overcome the burst release of small molecules from well-dispersed HAp nanoparticles by coating their drug-containing surface with a marine polymer, chitosan. At the same time, the antibacterial effectiveness of the given composite material and the osteoblastic cell response to it were analyzed. It was demonstrated that the embedment of 2–10 nm sized, narrowly dispersed HAp nanoparticles within the polymeric matrix mitigated the burst release of the small molecule model drug, fluorescein, bound to HAp by physisorption, and promoted zero-order release kinetics throughout most of the 3 weeks of release time, the time scale that falls in the range of the clinical optimality in the antibiotic treatment of osteomyelitis. The 24-h antibacterial efficacy against *S aureus* was, however, markedly lower for clindamycin-phosphate-loaded HAp/chitosan composites compared with the antibiotic-loaded HAp. Moreover, in sufficient concentrations, chitosan added to HAp inhibited the proliferation of the osteoblastic MC3T3-E1 cell line and reduced the excellent cell spreading and intimacy of the material/cell contact observed to take place upon incubation of the osteoblastic cells with pure HAp. This imperfect response was corroborated by the detected downregulation of osteocalcin and the transcription factor *Runx2* in cells incubated in the presence of HAp/chitosan composites. The peak in the expression of osteogenic markers paralleling the osteoblastic differentiation was also delayed most for the cell population incubated with HAp/chitosan particles. All in all, the positive effect of chitosan on the antibiotic elution profile of HAp nanoparticles as carriers for the controlled delivery of antibiotics in the treatment of osteomyelitis has had its drawbacks in terms of the lower bacteriostatic efficiency and the comparatively unviable osteoblastic cell response to the composite material, especially at higher dosages. Finally, as moderate inflammation is essential for normal regeneration,[90–92] regardless of the type of tissue in question, room should be left for the supposition that the relatively unviable response observed hereby with respect to HAp/chitosan *in vitro* may be reversed and even prove to be favorable in fostering bone regeneration in a more complex, *in vivo* biological setting.

Acknowledgments

References

1. Gogia JS, Meehan JP, Di Cesare PE, Jamali AA. Local antibiotic therapy in osteomyelitis. Sem Plastic Surg. 2009; 23(2):100–107.

2. Paluska SA. Osteomyelitis. Clin Fam Pract. 2004; 6(1):127–156.

3. Yenson A, de Fries HO, Deeb ZE. Actinomycotic osteomyelitis of the facial bones and mandible. Otolaryngol Head Neck Surg. 1983; 91(2):173–176. [PubMed: 6408574]

4. Hatzenbuehler J, Pulling TJ. Diagnosis and management of osteomyelitis. Am Fam Phys. 2011; 84(9):1027–1033.

5. Kurtz SM, Lau E, Schmier J, Ong KL, Zhao K, Parvizi J. Infection burden for hip and knee arthroplasty in the United States. J Arthroplasty. 2008; 23:984–991. [PubMed: 18534466]

6. Bozic KJ, Kurtz SM, Lau E, Ong K, Chiu V, Vail TP, Rubash HE, Berry DJ. The epidemiology of revision total knee arthroplasty in the United States. Clin Orthop Relat Res. 2010; 468(1):45–51. [PubMed: 19554385]

7. Harris I, Lyons M. Reoperation rate in diaphyseal tibia fractures. ANZ J Surg. 2005; 75:1041–1044. [PubMed: 16398806]

8. Uskokovi   V, Desai TA. Phase composition control of calcium phosphate nanoparticles for tunable drug delivery kinetics and treatment of osteomyelitis. Part 2: Antibacterial and osteoblastic response. J Biomed Mater Res A. 2013; 101(5):1427–1436. [PubMed: 23115128]

9. Uskokovi   V, Desai TA. Phase composition control of calcium phosphate nanoparticles for tunable drug delivery kinetics and treatment of osteomyelitis. Part 1: Preparation and drug release. J Biomed Mater Res A. 2013; 101(5):1416–1426. [PubMed: 23115118]

10. D'Este M, Eglin D. Hydrogels in calcium phosphate moldable and injectable bone substitutes: Sticky excipients or advanced 3-D carriers? Acta Biomater. 2013; 9(2013):5421–5430. [PubMed: 23201020]

11. Liu, SQ. Bioregenerative engineering: Principles and applications. Hoboken, New Jersey: John Wiley & Sons; 2007.

12. Smelcerovi   A, Knezevi -Jugovi   Z, Petronijevi   Z. Microbial polysaccharides and their derivatives as current and prospective pharmaceuticals. Curr Pharm Des. 2008; 14:3168–3195. [PubMed: 19075698]

13. Yin H, Du Y, Zhang J. Low molecular weight and oligomeric chitosans and their bioactivities. Curr Top Med Chem. 2009; 9:1546–1559. [PubMed: 19903163]

14. Arancibia R, Maturana C, Silva D, Tobar N, Tapia C, Salazar JC, Martínez J, Smith PC. Effects of chitosan particles in periodontal pathogens and gingival fibroblasts. J Dent Res. 2013; 92:740–745. [PubMed: 23788611]

15. Ing LY, Zin NM, Sarwar A, Katas H. Antifungal activity of chitosan nanoparticles and correlation with their physical properties. Int J Biomater. 2012:632698. [PubMed: 22829829]

16. Berknop-Schnurch A, Dunnhaupt S. Chitosan-based drug delivery systems. Eur J Pharm Biopharm. 2012; 81:463–469. [PubMed: 22561955]

17. Singha K, Namgung R, Kim WJ. Polymers in small-interfering RNA delivery. Nucleic Acid Ther. 2011; 21:133–147. [PubMed: 21749290]

18. Duceppe N, Tabrizian M. Advances in using chitosan-based nanoparticles for in vitro and in vivo drug and gene delivery. Expert Opin Drug Deliv. 2010; 7:1191–1207. [PubMed: 20836623]

19. Paul, W.; Sharma, CP. Natural bioresorbable polymers. In: Buchanan, F., editor. Degradation rate of bioresorbable materials. Cambridge, UK: Woodhead; 2008.

20. Yeh TH, Hsu LW, Tseng MT, Lee PL, Sonjae K, Ho YC, Sung HW. Mechanism and consequence of chitosan-mediated reversible epithelial tight junction opening. Biomaterials. 2011; 32(26): 6164–6173. [PubMed: 21641031]

21. Kowapradit J, Opanasopit P, Ngawhirunpat T, Rojanarata T, Ruktanonchai U, Sajomsang W. Methylated N-(4-N,N-dimethylaminocinnamyl) chitosan enhances paracellular permeability across Caco-2 cells. Drug Deliv. 2010; 17(5):301–312. [PubMed: 20302396]

22. Saper RB, Eisenberg DM, Phillips RS. Common dietary supplements for weight loss. Am Fam Physician. 2004; 70(9):1731–1738. [PubMed: 15554492]

23. Wilson OC Jr, Hull JR. Surface modification of nanophase hydroxyapatite with chitosan. Mater Sci Eng C. 2008; 28(3):434–437.

24. Lee HS, Tsai S, Kuo CC, Bassani AW, Pepe-Mooney B, Miksa D, Masters J, Sullivan R, Composto RJ. Chitosan adsorption on hydroxyapatite and its role in preventing acid erosion. J Colloid Interface Sci. 2012; 385:235–243. [PubMed: 22840874]

25. Chen J, Yu Q, Zhang G, Yang S, Wu J, Zhang Q. Preparation and biocompatibility of nanohybrid scaffolds by in situ homogeneous formation of nano hydroxyapatite from biopolymer polyelectrolyte complex for bone repair applications. Colloids Surf B Biointerfaces. 2012; 93:100–107. [PubMed: 22297206]

26. Tripathi A, Saravanan S, Pattnaik S, Moorthi A, Partridge NC, Selvamurugan N. Bio-composite scaffolds containing chitosan/nano-hydroxyapatite/nano-copper-zinc for bone tissue engineering. Int J Biol Macromol. 2012; 50(1):294–299. [PubMed: 22123094]

27. Tanase CE, Popa MI, Verestiuc L. Biomimetic chitosan-calcium phosphate composites with potential applications as bone substitutes: Preparation and characterization. J Biomed Mater Res B Appl Biomater. 2012; 100(3):700–708. [PubMed: 22121073]

28. Palazzo B, Gallo A, Casillo A, Nitti P, Ambrosio L, Piconi C. Fabrication, characterization and cell cultures on a novel composite chitosan-nano-hydroxyapatite scaffold. Int J Immunopathol Pharmacol. 2011; 24(1 Suppl 2):73–78. [PubMed: 21669142]

29. Thanyaphoo S, Kaewsrichan J. Synthesis and evaluation of novel glass ceramics as drug delivery systems in osteomyelitis. J Pharm Sci. 2012; 101(8):2870–2882. [PubMed: 22674208]

30. Zhang J, Wang C, Wang J, Qu Y, Liu G. In vivo drug release and antibacterial properties of vancomycin loaded hydroxyapatite/chitosan composite. Drug Deliv. 2012; 19:264–269. [PubMed: 22823893]

31. Ma T, Shang BC, Tang H, Zhou TH, Xu GL, Li HL, Chen QH, Xu YQ. Nano-hydroxyapatite/chitosan/konjac glucomannan scaffolds loaded with cationic liposomal vancomycin: Preparation, in vitro release and activity against *Staphylococcus aureus* biofilms. J Biomater Sci Polym Ed. 2011; 22(12):1669–1681. [PubMed: 21605505]

32. Shi P, Zuo Y, Li X, Zou Q, Liu H, Zhang L, Li Y, Morsi YS. Gentamicin-impregnated chitosan/nanohydroxyapatite/ethyl cellulose microspheres granules for chronic osteomyelitis therapy. J Biomed Mater Res A. 2010; 93(3):1020–1031. [PubMed: 19743510]

33. Zou Q, Li Y, Zhang L, Zuo Y, Li J, Li J. Antibiotic delivery system using nano-hydroxyapatite/chitosan bone cement consisting of berberine. J Biomed Mater Res A. 2009; 89(4):1108–1117. [PubMed: 18767062]

34. Fan J, Bi L, Wu T, Cao L, Wang D, Nan K, Chen J, Jin D, Jiang S, Pei G. A combined chitosan/nano-size hydroxyapatite system for the controlled release of icariin. J Mater Sci Mater Med. 2012; 23(2):399–407. [PubMed: 22083857]

35. Venkatesan P, Puvvada N, Dash R, Prashanth Kumar BN, Sarkar D, Azab B, Pathak A, Kundu SC, Fisher PB, Mandal M. The potential of celecoxib-loaded hydroxyapatite-chitosan nanocomposite for the treatment of colon cancer. Biomaterials. 2011; 32(15):3794–3806. [PubMed: 21392822]

36. Liu TY, Chen SY, Li JH, Liu DM. Study on drug release behaviour of CDHA/chitosan nanocomposites—Effect of CDHA nanoparticles. J Control Release. 2006; 112(1):88–95. [PubMed: 16530288]

37. Kim SW, Her SJ, Park SJ, Kim D, Park KS, Lee HK, Han BH, Kim MS, Shin CS, Kim SY. Ghrelin stimulates proliferation and differentiation and inhibits apoptosis in osteoblastic MC3T3-E1 cells. Bone. 2005; 37(3):359–369. [PubMed: 15978880]

38. Rousseau M, Boulzaguet H, Biagianti J, Duplat D, Milet C, Lopez E, Bedouet L. Low molecular weight molecules of oyster nacre induce mineralization of the MC3T3-E1 cells. J Biomed Mat Res A. 2007; 85A(2):487–497.

39. Celetti A, Testa D, Staibano S, Merolla F, Guarino V, Castellone MD, Iovine R, Mansueto G, Somma P, De Rosa G, Galli V, Melillo RM, Santoro M. Overexpression of the cytokine osteopontin identifies aggressive laryngeal squamous cell carcinomas and enhances carcinoma cell proliferation and invasiveness. Clin Cancer Res. 2005; 11(22):8019–1027. [PubMed: 16299231]

40. Pfaffl MW. A new mathematical model for relative quantification in real-time RT-PCR. Nucleic Acid Res. 2001; 29:e45. [PubMed: 11328886]

41. Onuma K, Ito A. Cluster growth model for hydroxyapatite. Chem Mater. 1998; 10(11):3346–3351.

42. Combes C, Rey C. Amorphous calcium phosphates: Synthesis, properties and uses in biomaterials. Acta Biomater. 2010; 6:3362–3378. [PubMed: 20167295]

43. He G, Dahl T, Veis A, George A. Nucleation of apatite crystals in vitro by self-assembled dentin matrix protein 1. Nat Mater. 2003; 2(8):552–558. [PubMed: 12872163]

44. Fosca M, Komlev VS, Yu A, Fedotov R, Rau Caminiti JV. Structural study of octacalcium phosphate bone cement conversion in vitro. ACS Appl Mater Interface. 2012; 4:6202–6210.

45. Lu HH, Pollack SR, Ducheyne P. Temporal zeta potential variations of 45S5 bioactive glass immersed in an electrolyte solution. J Biomed Mater Res. 2000; 51(1):80–87. [PubMed: 10813748]

46. Lee J, Yun KS, Choi CS, Shin SH, Ban HS, Rhim T, Lee SK, Lee KY. T cell-specific siRNA delivery using antibody-conjugated chitosan nanoparticles. Bioconjug Chem. 2012; 23(6):1174–1180. [PubMed: 22607555]

47. Fazil M, Md S, Hague S, Kumar M, Baboota S, Sahni JK, Ali J. Development and evaluation of rivastigmine loaded chitosan nanoparticles for brain targeting. Eur J Pharm Sci. 2012; 47:6–15. [PubMed: 22561106]

48. Narayanan D, Anitha A, Jayakumar R, Nair SV, Chennazhi KP. Synthesis, characterization and preliminary in vitro evaluation of PTH 1–34 loaded chitosan nanoparticles for osteoporosis. J Biomed Nanotechnol. 2012; 8:98–106. [PubMed: 22515098]

49. Amidi M, Mastrobattista E, Jiskoot W, Hennink WE. Chitosan-based delivery systems for protein therapeutics and antigens. Adv Drug Deliv Rev. 2010; 62:59–82. [PubMed: 19925837]

50. Hu CS, Chiang CH, Hong PD, Yeh MK. Influence of charge on FITC-BSA-loaded chondroitin sulfate-chitosan nanoparticles upon cell uptake in human Caco-2 cell monolayers. Int J Nanomed. 2012; 7:4861–4872.

51. Uskokovi V. Dynamic light scattering and microelec-trophoresis: Main prospects and limitations. J Dispersion Sci Technol. 2012; 33:1762–1786.

52. Caroni ALPF, de Lima CRM, Pereira MR, Fonseca JLC. Tetracycline adsorption on chitosan: A mechanistic description based on mass uptake and zeta potential measurements. Colloids Surf B. 2012; 100:222–228.

53. Ranjan OP, Shavi GV, Nayak UY, Arumugam K, Averineni RK, Meka SR, Sureshwar P. Controlled release chitosan microspheres of mirtazapine: *In vitro* and *in vivo* evaluation. Arch Pharm Res. 2011; 34:1919–1929. [PubMed: 22139691]

54. Saremi S, Atyabi F, Akhlaghi SO, Ostad SN, Dinarvand R. Thiolated chitosan nanoparticles for enhancing oral absorption of docetaxel: Preparation, in vitro and ex vivo evaluation. Int J Nanomed. 2011; 6:119–128.

55. Rajam M, Pulavendran S, Rose C, Mandal AB. Chitosan nanoparticles as a dual growth factor delivery system for tissue engineering applications. Int J Pharm. 2011; 410(1–2):145–152. [PubMed: 21392563]

56. Kim H, Tator CH, Shoichet MS. Chitosan implants in the rat spinal cord: Biocompatibility and biodegradation. J Biomed Mater Res A. 2011; 97:395–404. [PubMed: 21465644]

57. Ren D, Yi H, Wang W, Ma X. The enzymatic degradation and swelling properties of chitosan matrices with different degrees of N-acetylation. Carbohydr Res. 2005; 340:2403–2410. [PubMed: 16109386]

58. Correlo VM, Pinho ED, Pashkuleva I, Bhattacharya M, Neves NM, Reis RL. Water absorption and degradation characteristics of chitosan-based polyesters and hydroxyapatite composites. Macromol Biosci. 2007; 7:354–363. [PubMed: 17370274]

59. Zhou G, Li Y, Zhang L, Zuo Y, Jansen JA. Preparation and characterization of nano-hydroxyapatite/chitosan/konjac glucomannan composite. J Biomed Mater Res Part A. 2007; 83A(4):931–939.

60. Uskokovi V, Hoover C, Vukomanovi M, Uskokovi DP, Desai TA. Osteogenic and antimicrobial nanoparticulate calcium phosphate and/or poly-lactide-co-glycolide powders for the treatment of osteomyelitis. Mater Sci Eng C. 2013; 33(6):3362–3373.

61. Jarmila V, Vavrikova E. Chitosan derivatives with antimicrobial, antitumour and antioxidant activities—A review. Curr Pharm Des. 2011; 17(32):3596–3607. [PubMed: 22074429]

62. Ing LY, Zin NM, Sarwar A, Katas H. Antifungal activity of chitosan nanoparticles and correlation with their physical properties. Int J Biomater. 2012:632698. [PubMed: 22829829]

63. Chung Y-C, Su Y-P, Chen C-C, Jia G, Wang H-L, Wu JCG, Lin J-G. Relationship between antibacterial activity of chitosan and surface characteristics of cell wall. Acta Pharmacologica Sinica. 2004; 25:932–936. [PubMed: 15210068]

64. Butcher DT, Alliston T, Weaver VM. A tense situation: Forcing tumour progression. Nat Rev Cancer. 2009; 9:108–122. [PubMed: 19165226]

65. Uskokovi PS, Tang CY, Tsui CP, Ignjatovi N, Uskokovi D. Micromechanical properties of a hydroxyapatite/poly-L-lactide biocom-posite using nano-indentation and modulus mapping. J Europ Ceram Soc. 2007; 27:1559–1564.

66. Fan H, Wang L, Zhao K, Li N, Shi Z, Ge Z, Jin Z. Fabrication, mechanical properties, and biocompatibility of graphene-reinforced chitosan composites. Biomacromolecules. 2010; 11(9): 2345–2351. [PubMed: 20687549]

67. Liu H, Slamovich EB, Webster TJ. Increased osteoblast functions among nanophase titania/poly(lactide-co-glycolide) composites of the highest nanometer surface roughness. J Biomed Mater Res A. 2006; 78:798–807. [PubMed: 16741979]

68. Xu C, Yang F, Wang S, Ramakrishna S. *In vitro* study of human vascular endothelial cell function on materials with various surface roughness. J Biomed Mater Res A. 2004; 71:154–161. [PubMed: 15368265]

69. Rhoades J, Roller S. Antimicrobial actions of degraded and native chitosan against spoilage organisms in laboratory media and foods. Appl Environ Microbiol. 2000; 66(1):80–86. [PubMed: 10618206]

70. Jeevitha D, Amarnath K. Chitosan/PLA nanoparticles as a novel carrier for the delivery of anthraquinone: Synthesis, characterization and *in vitro* cytotoxicity evaluation. Colloids Surf B. 2013; 101(1):126–134.

71. Ma Z, Lim LY. Uptake of chitosan and associated insulin in Caco-2 cell monolayers: A comparison between chitosan molecules and chitosan nanoparticles. Pharm Res. 2003; 20:1812–1819. [PubMed: 14661926]

72. Loh JW, Saunders M, Lim LY. Cytotoxicity of monodispersed chitosan nanoparticles against the Caco-2 cells. Toxicol Appl Pharmacol. 2012; 262(3):273–282. [PubMed: 22609640]

73. Loh JW, Yeoh G, Saunders M, Lim LY. Uptake and cytotoxicity of chitosan nanoparticles in human liver cells. Toxicol Appl Pharmacol. 2010; 249:148–157. [PubMed: 20831879]

74. Loretz B, Bernkop-Schnurch A. In vitro cytotoxicty testing of non-thiolated and thiolated chitosan nanoparticles for oral gene delivery. Nanotoxicology. 2007; 1:139–148.

75. Chae SY, Jang MK, Nah JW. Influence of molecular weight on oral absorption of water soluble chitosans. J Control Release. 2005; 102:383–394. [PubMed: 15653159]

76. Opanasopit P, Aumklad P, Kowapradit J, Ngawhiranpat T, Apirakaramwong A, Rojanarata T, Puttipipatkhachorn S. Effect of salt forms and molecular weight of chitosans on in vitro permeability enhancement in intestinal epithelial cells (Caco-2). Pharm Dev Technol. 2007; 12:447–455. [PubMed: 17963144]

77. Qi LF, Xu ZR, Li Y, Jiang X, Han XY. In vitro effects of chitosan nanoparticles on proliferation of human gastric carcinoma cell line MGC803 cells. World J Gastroenterol. 2005; 11:5136–5141. [PubMed: 16127742]

78. Carreno-Gomez B, Duncan R. Evaluation of the biological properties of soluble chitosan and chitosan microspheres. Int J Pharm. 1997; 148:231–240.

79. Baldrick P. The safety of chitosan as a pharmaceutical excipient. Regul Toxicol Pharmacol. 2010; 56:290–299. [PubMed: 19788905]

80. Chaudhury A, Das S. Recent advancement of chitosan-based nanoparticles for oral controlled delivery of insulin and other therapeutic agents. AAPS PharmSciTech. 2011; 12:10–20. [PubMed: 21153572]

81. Tanaka Y, Tanioka S, Tanaka M, Tanigawa T, Kitamura Y, Minami S, Okamoto Y, Miyashita M, Nanno M. Effects of chitin and chitosan particles on BALB/c mice by oral and parenteral administration. Biomaterials. 1997; 18:591–595. [PubMed: 9134158]

82. Cheng Q, Zhang J, Xia W. Prenatal and developmental effect of high molecular weight chitosan (HMWCS) to mice. Regul Toxicol Pharmacol. 2013; 65(3):294–303. [PubMed: 23321397]

83. Hu YL, Qi W, Han F, Shao JZ, Gao JQ. Toxicity evaluation of biodegradable chitosan nanoparticles using a zebrafish embryo model. Int J Nanomed. 2011; 6:3351–3359.

84. Peng H, Yin Z, Liu H, Chen X, Feng B, Yuan H, Su B, Ouyang H, Zhang Y. Electrospun biomimetic scaffold of hydroxyapatite/chitosan supports enhanced osteogenic differentiation of mMSCs. Nanotechnology. 2012; 23:495102, 10. [PubMed: 23149806]

85. Kim B-S, Kim JS, Chung YS, Sin Y-W, Ryu K-H, Lee J, You H-K. Growth and osteogenic differentiation of alveolar human bone marrow-derived mesenchymal stem cells on chitosan/hydroxyapatite composite fabric. J Biomed Mater Res A. 2012; 101(6):1550–1558. [PubMed: 23135904]

86. Phan TCA, Xu J, Zheng MH. Interaction between osteoblast and osteoclast: Impact in bone disease. Histol Histopathol. 2004; 19:1325–1344. [PubMed: 15375775]

87. Wenk H-R, Heidelbach F. Crystal alignment of carbonated apatite in bone and calcified tendon: Results from quantitative texture analysis. Bone. 1999; 24:361–369. [PubMed: 10221548]

88. Patel LN, Zaro JL, Shen WC. Cell penetrating peptides: Intracellular pathways and pharmaceutical perspectives. Pharm Res. 2007; 24:1977–1992. [PubMed: 17443399]

89. Huang W, Carlsen B, Rudkin G, Berry M, Ishida K, Yamaguchi DT, Miller TA. Osteopontin is a negative regulator of proliferation and differentiation in MC3T3-E1 pre-osteoblastic cells. Bone. 2004; 34(5):799–808. [PubMed: 15121011]

90. Mountziaris PM, Spicer PP, Kasper FK, Mikos AG. Harnessing and modulating inflammation in strategies for bone regeneration. Tissue Eng Part B Rev. 2011; 17(6):393–402. [PubMed: 21615330]

91. Benowitz LI, Popovich PG. Inflammation and axon regeneration. Curr Opin Neurol. 2011; 24(6):577–583. [PubMed: 21968547]

92. Thomas MV, Puleo DA. Infection, inflammation, and bone regeneration: A paradoxical relationship. J Dent Res. 2011; 90(9):1052–1061. [PubMed: 21248364]
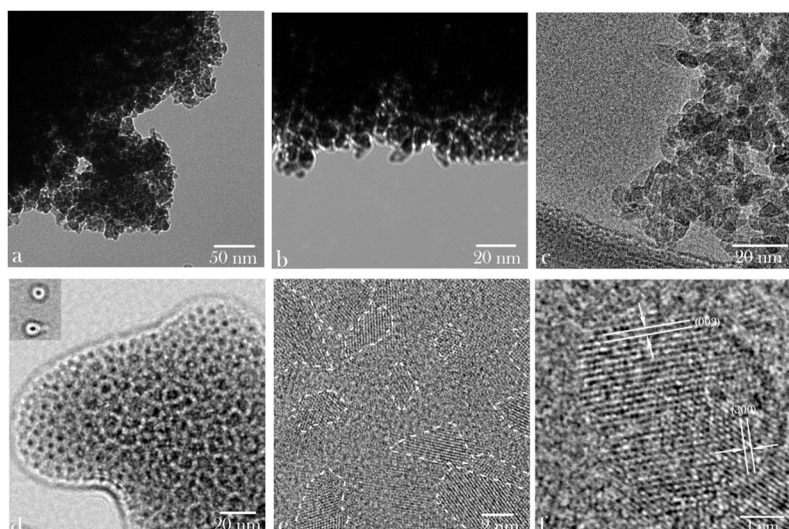
Figure 1.
Transmission electron micrographs of pure HAp (a–c) and of HAp/chitosan composites (d–
f) at different magnifications. Outlines of some of the crystalline domains interspersed
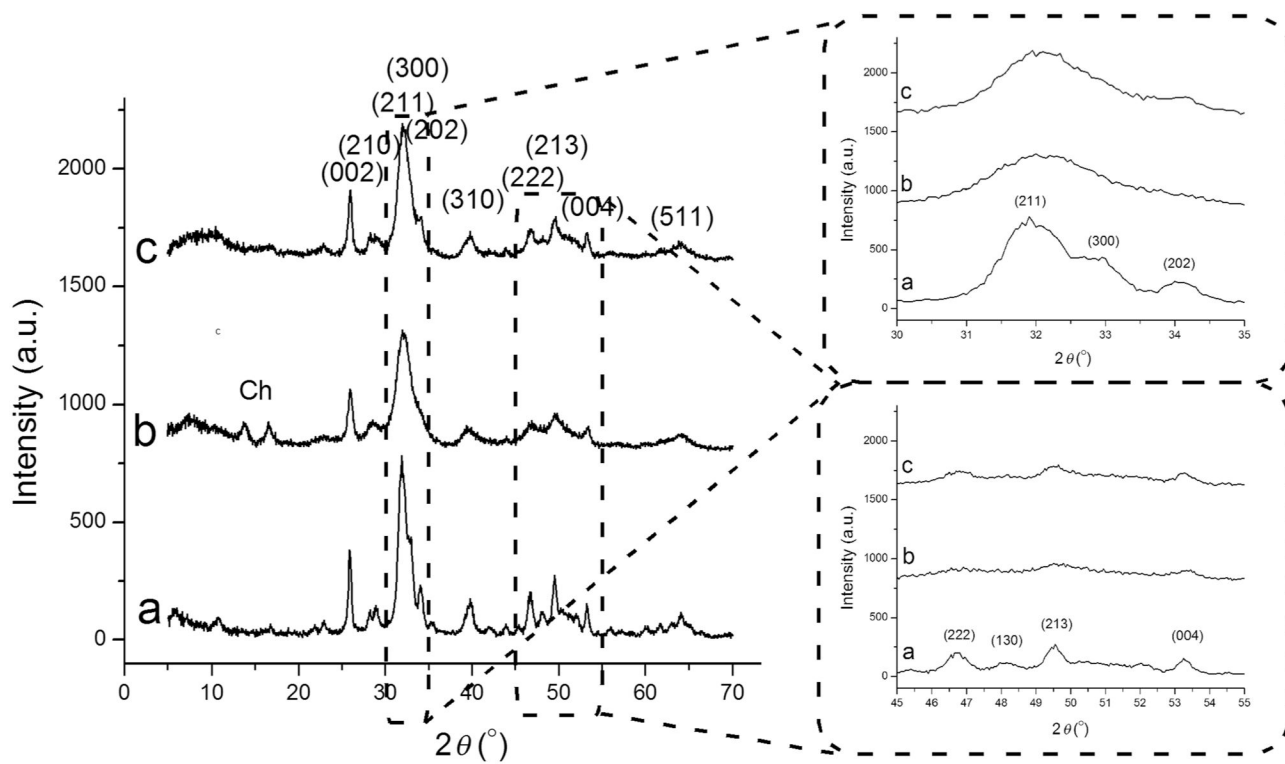within the amorphous polymeric phase are shown in (e).

Figure 2.
X-ray diffractograms of HAp (a), HAp/chitosan (b), and clindamycin-loaded HAp (c) powders synthesized in this study, along with {hkl}indices ascribed to the most intensive reflections of crystalline HAp. Diffraction peaks originating from chitosan are labeled with "Ch." The two inlets show magnified $2\theta = 30°–35°$ and $45°–55°$ regions.
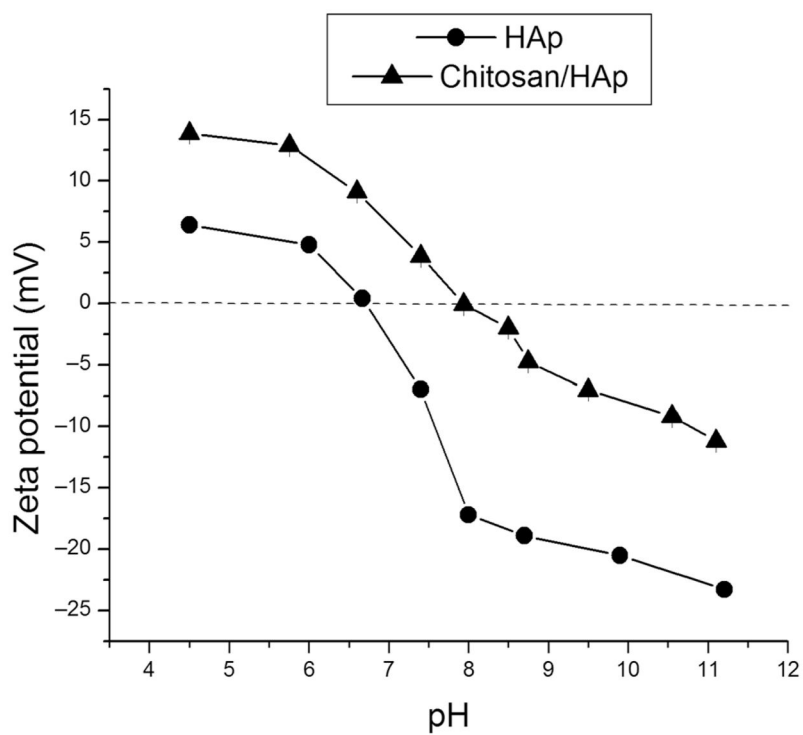
Figure 3.
Comparative ξ-potential versus pH curves for HAp and HAp/chitosan nanoparticles in 20 mM Tris–HCl, alongside different ξ-potential values at pH 7.4 and IEPs for pure HAp, as-prepared HAp/chitosan composites, and HAp/chitosan composites following the 3-week degradation period.
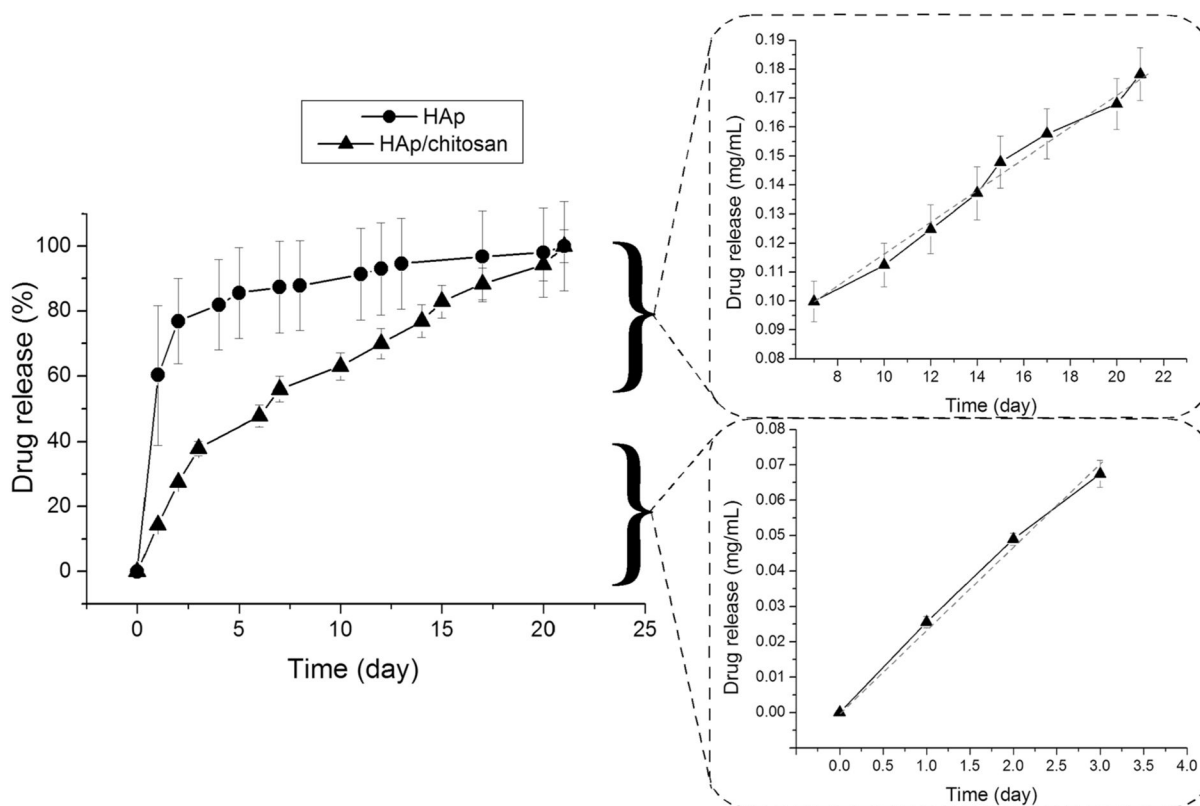
Figure 4.
Comparative profiles for the cumulative drug release of fluorescein from HAp nanoparticles
(-●-) and HAp/chitosan composites (-▲-), and fitting of the release curve of fluorescein
from HAp/chitosan composites (-▲-) for the first 72 h and for the period between 7 and 21
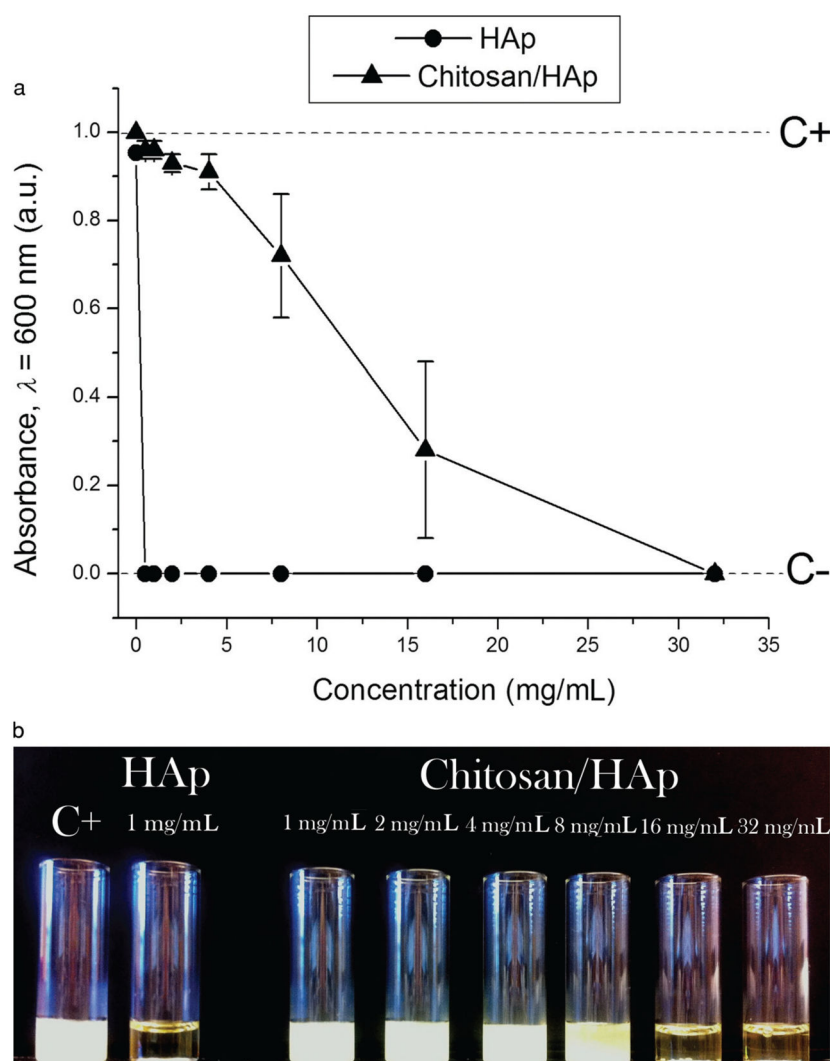days to the zero-order kinetics (dashed red lines).

Figure 5.
Optical transparence at $\lambda = 600$ nm (a) and visual appearance (b) of BHI broths inoculated with S *aureus* (10^5 bacteria per milliliter) and different amounts of clindamycin-loaded HAp (-●-) and HAp/chitosan (-▲-) powders, following 24 h incubation at 37°C. C− dashed line denotes the absorbance of the negative control, incubated without any added bacteria, whereas C+ dashed line indicates the absorbance of the positive control, incubated with 10^5 bacteria per milliliter and no antibiotic-loaded particles.
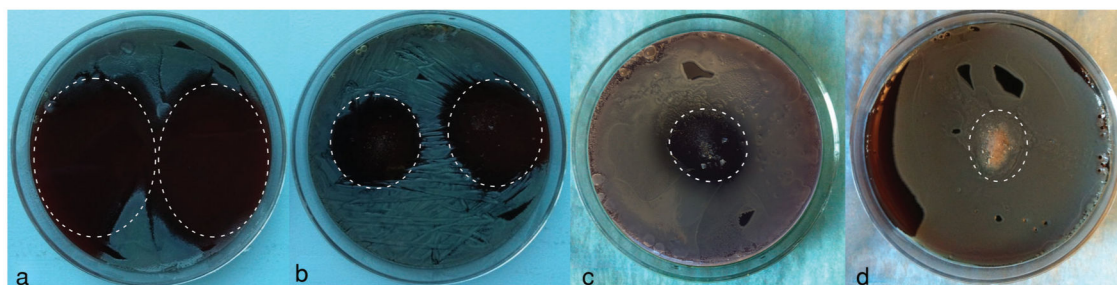
Figure 6.
Inhibition zones formed around 1 mg of clindamycin (a), 1 mg of clindamycin-loaded HAp particles (b), 5 mg of clindamycin-loaded HAp/chitosan particles (c), and 50 mg of HAp/chitosan particles (d) on sheep blood agar plates seeded with 7×10^3 S *aureus* bacteria per mm^2 following an overnight incubation. The area around the deposited powders is encircled with a dashed line.
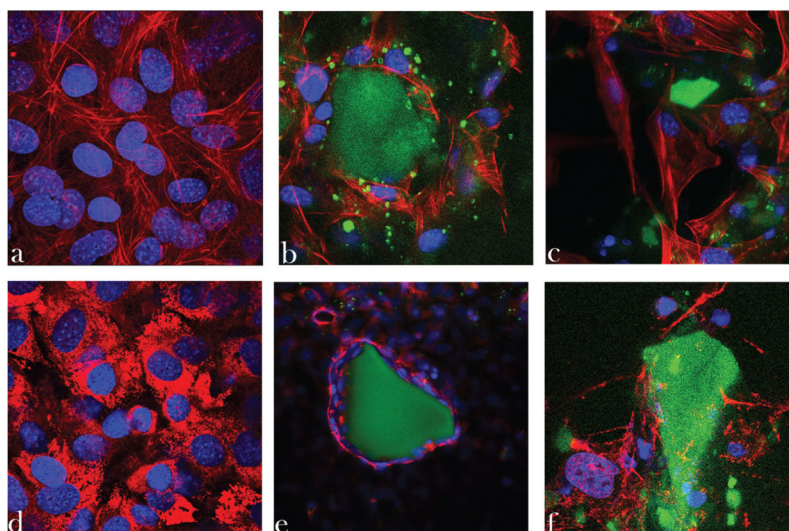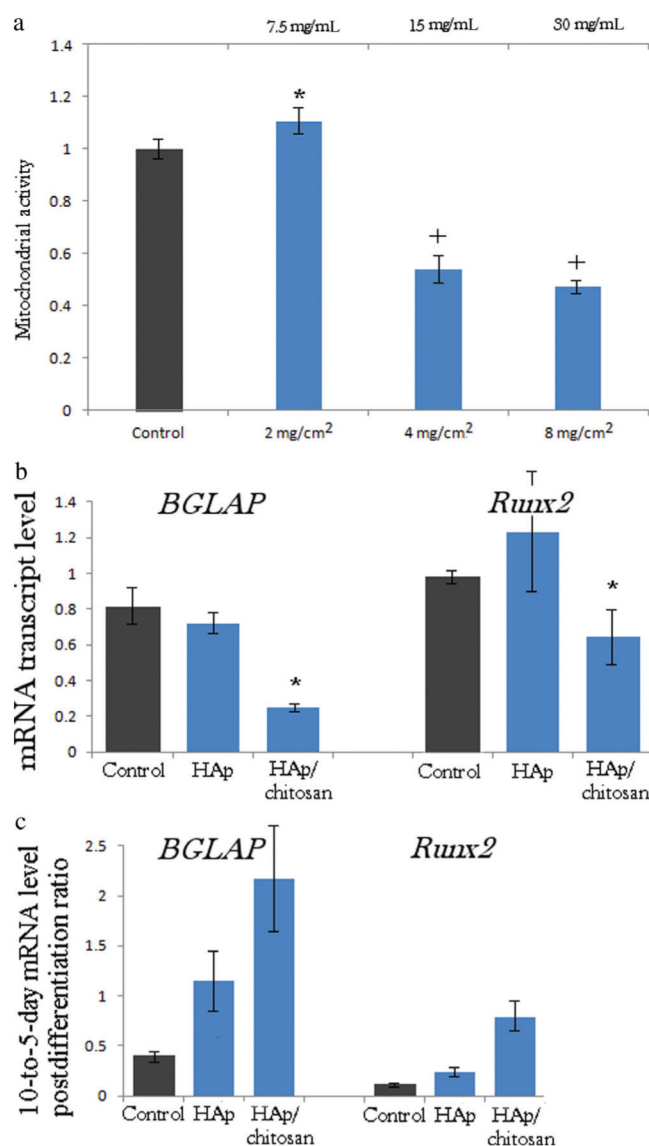
Figure 7.
Single-plane confocal optical micrographs of fluorescently stained osteoblastic MC3T3-E1 cells [cytoskeletal f-actin (a–c) or type I collagen (d–f)—red; nucleus—blue] of the control sample (a and d) and of those incubated with HAp nanoparticles (b and e) and HAp/chitosan composites (c and f) (both green), following 5 days of incubation. The sizes of the images are $270 \times 270 \ \mu m^2$ (a–d and f) or $450 \times 450 \ \mu m^2$ (e).

Figure 8.

(a) Mitochondrial dehydrogenase activity indicative of cell viability normalized to the negative control (C–) and determined by the MTT assay after 96 h of incubation with different HAp/chitosan particle concentrations normalized to surface area of confluent MC3T3-E1 osteoblastic cells (mg/cm^2) and to the volume of the cell culture medium (mg/mL). Data normalized to the optical density at $\lambda = 570$ nm of the negative control are shown as arithmetic means with error bars representing SD. Samples with significantly ($p < 0.05$ with respect to the control group) higher cell viability with respect to the control are marked with a*, whereas those with significantly lower cell viability are marked with a+. (b) The comparative effect of HAp and HAp/chitosan nanoparticulate powders on the mRNA expression of osteogenic markers *BGLAP* and *Runx2* in osteoblastic MC3T3-E1 cells. mRNA expression was detected by quantitative real-time PCR relative to the housekeeping gene *ACTB*. Data normalized to expression of *ACTB* are shown as averages with error bars

representing SD. Genes significantly ($p < 0.05$) downregulated with respect to the control group are marked with *. (c) 10-to-5-day postdifferentiation ratio in the mRNA expression level detected by quantitative real-time PCR relative to the housekeeping gene *ACTB*. All data groups are significantly different ($p < 0.05$) from the control.

Table 1

Primer Pair Sequences Used for the qPCR Analysis

Gene	Forward 5′–3′ Primer	Reverse 5′–3′ Primer
ACTB	GGCCCAGAGCAAGAGAGGTATCC	ACGCACGATTTCCCTCTCAGC
BSP-1	AGGAGGAGGCAGAGCACA	CTGGTATGGCACAGGTGATG
BGLAP	CTCACAGATGCCAAGCCCA	CCAAGGTAGCGCCGGAGTCT
Runx2	AAATGCCTCCGCTGTTATGAA	GCTCCGGCCCACAAATCT

Table 2

The Measured ξ-Potential and IEP Values for Pure HAp and HAp/Chitosan Composites Before and After the Drug Release Experiment

	HAp	As-Prepared HAp/Chitosan	Postdegradation HAp/Chitosan
ξ-Potential (mV)	−7.0	3.9	0.9
IEP	6.7	7.9	7.5